ELSEVIER

Materials Science and Engineering A 466 (2007) 207–217

MATERIALS SCIENCE & ENGINEERING A

www.elsevier.com/locate/msea

Cyclic deformation and dynamic compressive properties of copper bicrystals

R.Q. Yang *, S.X. Li, Z.F. Zhang

Shenyang National Laboratory for Materials Science, Institute of Metal Research, The Chinese Academy of Sciences, Shenyang 110016, China

Received 17 August 2006; received in revised form 12 February 2007; accepted 19 February 2007

Abstract

Cyclic deformation and dynamic compressive tests of three copper bicrystals were carried out on a Shimadzu servo-hydraulic testing machine and a split Hopkinson pressure bar (SHPB) apparatus respectively. The post-deformation dislocation structures, grain boundary (GB) serrations and adiabatic shear bands (ASBs) were examined using electron channeling contrast (ECC) imaging in a scanning electron microscope (SEM). After cyclic straining the secondary slip bands were activated near the GB forming a GB affected zone (GBAZ). Microstructures beneath it are dislocation labyrinth or irregular persistent slip bands (PSBs). The saturation stress at GBAZ was calculated to be higher than that in the grain interior. In dynamic compression, the formation of ASBs, was found to be promoted by the GB. Dynamic stress–strain curves were compared with each other for single crystals, bicrystals and polycrystals. Microstructures were also characterized with orientation imaging microscopy (OIM) by electron backscattering diffraction (EBSD) technique. It was found that relatively larger lattice rotations occurred across the ASBs than in the other regions, which can be deduced by the localization of simple shear along ASBs. No recrystallization was found in the ASBs or along GBs in the present circumstance.

Keywords: Copper bicrystal; Grain boundary; Cyclic straining; EBSD; Dynamic deformation; Lattice rotation; Adiabatic shear bands

1. Introduction

The role of grain boundaries in plastic deformation has long been an interesting subject and regained increased attention [1–7]. It is well known that with decreasing grain size, the volume fraction of grain boundary (GB) increases significantly. Therefore, GB becomes a controlling factor in the plastic deformation of fine-grained polycrystals. To clarify the GB effects, different kinds of bicrystals, such as aluminum [1,6,8,9], Fe-alloys [4,10,11] and copper [12–15], have been widely employed in the cyclic straining or monotonic loading at low strain rates. Experimental results reveal that large angle random GBs become the preferential sites to initiate fatigue crack during cyclic straining, independent of the interaction angle between the GB plane and the stress axis due to the piling-up of dislocations [15] and there was a GB affected zone (GBAZ) in the vicinity of a GB [6,8,13–15]. GB influences the deformation mode and the mechanical properties of polycrystalline materials to a great extent.

On the other hand, engineering materials are often subjected to high strain rate loadings such as high-speed machining, ballistic impact, metal punching and forging. At high strain rates, materials often exhibit deformation instability characterized by the formation of adiabatic shear bands (ASBs) which have different deformation and fracture behaviors in comparison with those occurred under quasi-static or low strain rate loading. Profuse investigations of high strain rate responses of materials are concentrated on polycrystalline materials [16–24]. The experiments indicated that high strain rate deformation instability and the formation of ASBs seem to be strongly dependent on the sample geometry and mechanical properties of a material rather than its local crystallography [18]. Recent studies even found that the ASBs could not be initialized without material inhomogeneity or geometry inhomogeneity [21]. However, to some extent GB can be regarded as a kind of material inhomogeneity, its effect on the high strain rate deformation is not clearly known yet. There may be two reasons. One is that the mechanical effects or the geometry inhomogeneity are severer than the GB's effect.

* Corresponding author. Fax: +86 24 23971215.
E-mail address: rqyang@imr.ac.cn (R.Q. Yang).

0921-5093/$ – see front matter © 2007 Elsevier B.V. All rights reserved.
doi:10.1016/j.msea.2007.02.066

For example, in the hat-shaped specimen method [22], the specimens were machined so that intense pure shear stress can be imposed on a narrow region. During dynamic process, ASBs are forced to generate within this region. In this circumstance, GB's effect is 'covered up' by the geometrical effect. Another reason may be that the width of ASBs (about 2–200 μm) often covers the conventional grain size range (5–50 μm). It is hardly for one single GB to manifest its contribution on the dynamic deformation in the polycrystalline materials. Therefore, the contributions of a single GB on the dynamic compression are still not clear.

Furthermore, preferential dynamic recrystallization (DRX) nucleation at the grain boundary on Cu–Si bicrystals at 1023 K was observed at strain rates from 4×10^{-5} to $4 \times 10^{-3}\ s^{-1}$ [25]. DRX is also found in the ASBs in the ballistic impact at the strain rate above 10^5 [21–23]. However, investigations of DRX at the strain rate about 10^3–$10^4\ s^{-1}$ at room temperature are still rare. In the present paper, copper bicrystals with random GB parallel to the loading axis were tested in the strain rate about $4 \times 10^3\ s^{-1}$. The non-existence of DRX, GB serration, dislocation rearrangement and GB's effect on ASB formation along with bicrystals' cyclic deformation properties are reported.

2. Experiments

Bicrystal plates with the size of 10 mm × 55 mm × 260 mm were grown from OFHC copper of 99.999% purity by the Bridgman method. Specimens with the dimension of 7.5 mm × 5 mm × 60 mm were cut from the plates. Three different bicrystals B1, B2 and B3 were prepared with the gauge section of 5 mm × 5 mm × 20 mm. The specimens were carefully electro-discharge machined to make sure that the GB was in the center and parallel to the loading axis. Prior to the fatigue test, the specimens were mechanically and electrolytically polished on all surfaces to ensure that a strain-free and smooth surface layer was obtained.

Push–pull fatigue tests were conducted at room temperature in air using a Shimadzu servo-hydraulic testing machine with a constant axial plastic strain amplitude of 1.5×10^{-3}. A triangular waveform with a frequency of 0.2 Hz was employed and the tests were terminated after saturation at about 10^4 cycles. Then the surface slip morphology was observed. Afterwards, those surface slip traces were removed and repolished to examine the dislocation patterns, especially near the GB, by the scanning electron microscope (SEM)-electron channeling contrast (ECC) technique [26].

After fatigue the gauge section of the specimens was cut into pieces with a dimension of 5 mm × 5 mm × 4 mm then repolished and used for dynamic tests. Why we use fatigued specimens for dynamic tests, the reasons are as follows: (1) during pre-cyclic straining the dislocation patterns were well developed, which can serve as markers to indicate the deformation process during dynamic loading. (2) The ASBs can occur rather easily in the fatigued single crystals compared with the counterparts without pre-cyclic straining [26]. (3) In practice, a metal component may undergo intense cyclic deformation before impact. Therefore, it is necessary to study the dynamic behavior of fatigued specimens.

Those specimens with pre-cyclic straining were named with prefix 'CS'. According to the finial impact axial strain, specimens of this group, say B1, were named as CS-B1-1, CS-B1-2 and CS-B1-3, with the final strains of −0.138, −0.178 and −0.283, respectively. For comparison, another group of bicrystal B1 with the dimension of 5 mm × 5 mm × 4 mm was also prepared. They did not receive pre-cyclic straining treatment before dynamic tests. They were named as UC-B1-1, UC-B1-2 and UC-B1-3 with the final strains of −0.135, −0.197 and −0.215, respectively.

Dynamic compressive tests were conducted on a split Hopkinson pressure bar (SHPB) apparatus. The specimens were assembled between the incident bar and transmitter bar. The strain rate was adjusted to be about 4×10^3 for all the specimens. Before tests, thick steel tubes of different lengths were mounted outside the specimens. Therefore, the incident bar could be immediately stopped after it contacted the steel tube. In the present tests, the total engineering strains in the range of 10–30% could be obtained.

After dynamic tests, all the specimens were examined in a Cambridge S-360 SEM with ECC technique. The orientation imaging microscopy (OIM) by electron backscattering diffraction (EBSD) technique was conducted with a step of 0.5 μm in a field emission scanning electron microscope (FESEM) of LEO Supra 35.

3. Results and discussion

3.1. Bicrystals' orientations

The axial orientations of the three bicrystals were determined by EBSD technique, as listed in Table 1. The axial orientations of the two component grains of bicrystal B1 are $[\bar{2}\,5\,8]$ and $[\bar{1}\,15\,20]$, respectively, with a misorientation of 10.8°. For bicrystals B2 and B3, the misorientations of the two component grains are 8.5° and 10.2°, respectively. Their orientations are also shown in the standard stereographic triangle (Fig. 1). For bicrystal B1 the component grain G1 orients typically single-slip and is close to $[\bar{1}\,3\,5]$ (less than 2.5°), and grain G2 is close to [0 3 4] double slip orientation (also less than 2.5°) that is at [0 0 1]–[0 1 1] side. For bicrystal B2, both grains G1 and G2 orient for single-slip. For bicrystal B3, the component grain G2 is rather close to the $[\bar{1}\,1\,7]$ double slip orientation (about 8°). As can be seen above, for all three bicrystals, their two component grains have almost same misorientations (8–10°) but orient differently. Their saturation stresses and initial harden rates vary a great deal as presented in the following section.

3.2. Cyclic hardening and saturation behavior

Fig. 2 shows the cyclic hardening and saturation curves of the three bicrystals. All the bicrystals display a typical rapid cyclic hardening and then cyclic saturation behavior. Their axial saturation stresses differ from 62 to 72 MPa (Fig. 2(a)). This

Table 1
Bicrystals' orientations and cyclic straining data

Specimen no.	Orientation	Pri. Ω	Ω_B	Sec. Ω	Ω'_B	Ω_B/Ω'_B	τ_s[a] (MPa)	$\theta_{0.2}$ (MPa)
B1								
G1	[$\bar{2}$ 5 8]	0.483	0.474	0.395	0.419	1.13	29.4	28.4
G2	[$\bar{1}$ 15 20]	0.466		0.446				
B2								
G1	[$\bar{3}$ 13 21]	0.490	0.492	0.439	0.439	1.12	30.6	38.9
G2	[$\bar{3}$ 7 16]	0.494		0.439				
B3								
G1	[$\bar{1}$ 3 6]	0.497	0.489	0.444	0.445	1.10	35.1	58.5
G2	[$\bar{4}$ 7 24]	0.481		0.446				

[a] τ_s is the bicrystals' saturation shear stress.

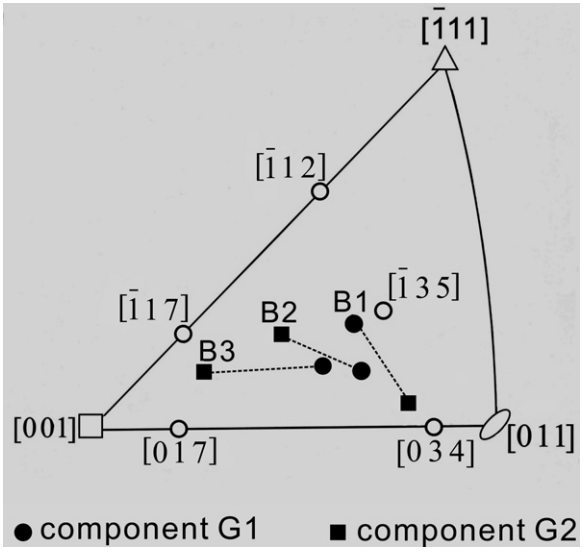

Fig. 1. Bicrystals' axial orientations in the standard stereographic triangle.

is mostly due to the different GB strengthening effects and the different orientations of component grains.

The Schmid factor Ω is widely used to calculate the resolved shear stress of single crystals from the imposed axial stress. For a bicrystal with two component grains G1 and G2 combined in parallel, Zhang et al. [13] proposed an orientation factor Ω_B to consider component orientations' effect on the saturation stress, which can be described as,

$$\Omega_B = \left(\frac{V_{G1}}{\Omega_{G1}} + \frac{V_{G2}}{\Omega_{G2}}\right)^{-1} \quad (1)$$

Here, V_{G1} and V_{G2} are the volume fractions of component grains G1 and G2, respectively. Ω_G is the primary Schmid factor in each grain. For the present bicrystal B1, $V_{G1} = V_{G2} = 0.5$, and $\Omega_{G1} = 0.483$, $\Omega_{G2} = 0.466$. Substituting these values into Eq. (1), gives $\Omega_B = 0.474$. For bicrystal B2 and B3 their Ω_B are 0.492 and 0.489, respectively, as listed in Table 1. With Ω_B, the bicrystals' plastic shear strain amplitudes γ_{pl} (Fig. 2(b)) and saturation shear stresses in the cyclic straining can be calculated and the latter are also listed in Table 1. Furthermore, the accumulative plastic shear strain $\gamma_{pl,cum}$ for bicrystals can be obtained ($\gamma_{pl,cum} = 4N\gamma_{pl}$, N is the number of cycles).

Considering the volume fractions of GBAZ of the bicrystals, the total force acting on the specimen can be given by the sum of the forces acting on the particular volumes. Therefore, the saturation stress of bicrystal, σ^B_{sa}, can be written as:

$$\sigma^B_{sa} = \{\sigma^{G1}_{sa}(V_{G1} - V^{GBAZ1}) + \sigma^{G2}_{sa}(V_{G2} - V^{GBAZ2})\} + (\sigma^{GBAZ1}_{sa} V^{GBAZ1} + \sigma^{GBAZ2}_{sa} V^{GBAZ2}) \quad (2)$$

Here, σ^G_{sa} is the saturation stress acting at grain interior away from GBAZ. σ^{GBAZ}_{sa} is the saturation stress acting at the GBAZ, V^{GBAZ} is the volume fraction of the GBAZ in each component grain. The first part of Eq. (2) represents the saturation stress carried

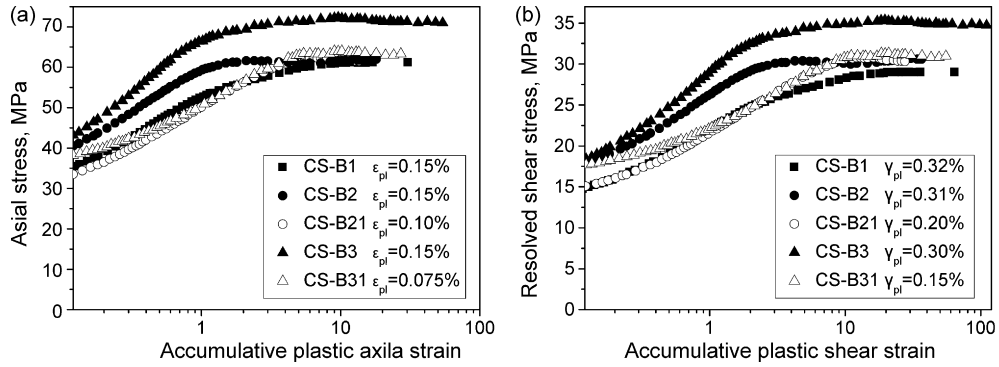

Fig. 2. The cyclic hardening curves at different strain amplitudes of the three bicrystals. (a) The axial stress vs. accumulative plastic axial strain ($4N\varepsilon_{pl}$). (b) The resolved shear stress vs. accumulative plastic shear strain ($4N\gamma_{pl}$).

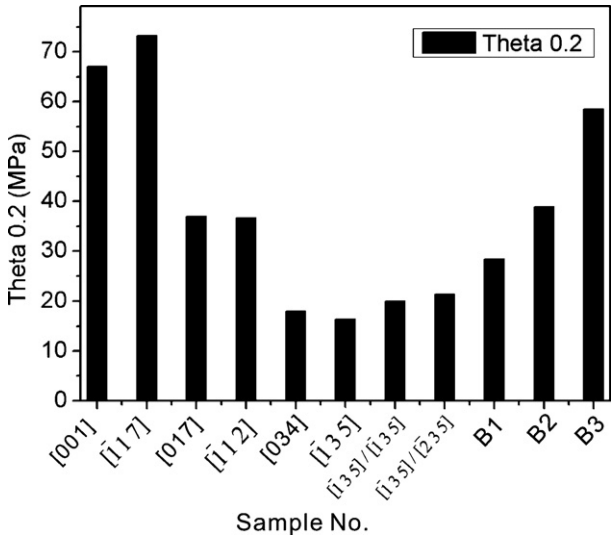

Fig. 3. The initial hardening rates of some copper single crystals and bicrystals at shear strain amplitude about 0.3%. Note that the data of [$\bar{1}$ 3 5], [$\bar{1}$ 3 5]/[$\bar{1}$ 3 5], [$\bar{1}$ 3 5]/[$\bar{2}$ 3 5] bicrystals were obtained at plastic shear strains amplitude of 0.4%.

by the grain interior and the second part represents those carried by GBAZ. In each component grain interior $\sigma_{sa}^{G} = \tau_{sa}^{PSB}/\Omega_G$, therefore, Eq. (2) can be transformed as follows:

$$\sigma_{sa}^{B} = \tau_{sa}^{PSB}\left\{\left(\frac{V_{G1} - V^{GBAZ1}}{\Omega_{G1}}\right) + \left(\frac{V_{G2} - V^{GBAZ2}}{\Omega_{G2}}\right)\right\} + (\sigma_{sa}^{GBAZ1} V^{GBAZ1} + \sigma_{sa}^{GBAZ2} V^{GBAZ2}) \quad (3)$$

Here, τ_{sa}^{PSB} is the saturation shear stress acting at persistent slip bands (PSBs) and equal to 28–30 MPa [27–29]. For bicrystal B1, its saturation stress σ_{sa}^{B} is equal to 62 MPa. GBAZ only occurred in the G2 component and it is approximately 1 mm in width. Therefore, $V^{GBAZ1} = 0$, $V^{GBAZ2} = 0.2$, Ω_{G1} and Ω_{G2} are known to be 0.483 and 0.466, respectively. The saturation stress at GBAZ in bicrystal B1 can be calculated as 76 MPa ($\tau_{sa}^{PSB} = 28$ MPa was used in the calculation). For bicrystals B2 and B3, the saturation stresses at GBAZs are 108 and 158 MPa, respectively. For the polycrystal copper its saturation stress at the same strain amplitude is about 120–140 MPa [30]. The calculated stresses at GBAZs cover these values. It is rational that with grain size decreasing, the volume fraction of GBAZs will increase and it will carry most of imposed stress. Therefore, polycrystals' saturation stresses can be very close to those acting at GBAZs.

The initial hardening rate $\theta_{0.2}$ ($\theta_{0.2} = \Delta\tau/\Delta\gamma_{pl,cum}$, $\Delta\gamma_{pl,cum} = 0.2$) is often calculated to describe the cyclic hardening behavior. The values of $\theta_{0.2}$ for three bicrystals are listed in Table 1. A comparison between present and previous data of different single crystals and bicrystals with GBs parallel to the loading axis [31–35] is made as shown in Fig. 3. The initial hardening rates of all bicrystals are pretty larger than the mean values of those with their component grains, indicating a considerable accelerating effect of GBs on the initial hardening process of crystals. For bicrystal B1, $\theta_{0.2}$ is 28.4 MPa and as mentioned above, its component grains orient very closely to the [$\bar{1}$ 3 5] and [0 3 4], respectively. As can be seen from Fig. 3 the mean value of $\theta_{0.2}$ for [$\bar{1}$ 3 5] and [0 3 4] single crystals is as large as 17.2 MPa. It is pretty lower than that of bicrystal B1. Similarly, $\theta_{0.2}$ of bicrystal B3 (58.5 MPa) is larger than the average value (45 MPa) of those for [$\bar{1}$ 3 5] and [$\bar{1}$ 1 7] single crystals. Other cases are also analogous.

3.3. Surface slip morphology and dislocation patterns

During cyclic straining, secondary slips were activated near the GB because of the serious stress–strain incompatibility as can be seen in Fig. 4. In the present circumstance secondary slips only occur in one component grain. The total number of activating slip systems are 3 or 4 for different bicrystals. In the vicinity of GB, primary slip lines are regularly modulated by the other slip lines forming a GBAZ. For bicrystal B1 the primary and secondary slip lines emerge alternately in the GBAZ to form a cross-weaved structure. However, for bicrystal B3, Their two secondary slips and primary slips emerge simultaneously to form a parallelogram network.

The dislocation patterns near the GB of bicrystal B1 are shown in Fig. 5(a and b). As pointed out in the previous section, the component grain G1 [$\bar{2}$ 5 8] of bicrystal B1 orients for typical single-slip. After fatigue the dislocation patterns consist of two-phase structures, i.e. PSBs with dislocation ladder structure embedded in matrix veins [36,37], as shown in the upper part of Fig. 5(a and b). Its component grain G2 [$\bar{1}$ 15 20] is rather close to [0 0 1]–[0 1 1] double slip side, the dislocation patterns after fatigue are labyrinth structures and irregular PSBs. This feature can be seen in the lower part of Fig. 5(a and b), which is consistent with other report [38]. However, this feature extends only about 1 mm away form GB in the lower grain. That is approximately equal to the width of GBAZ, see Fig. 5(c). Apart from GBAZ, the dislocation patterns gradually turn into the regular PSBs and veins, i.e. two-phase structure. Similar dislocation patterns can be observed in bicrystal B2 (Fig. 5(d–f)) and bicrystal B3.

3.4. Dynamic compressive stress–strain curves

The dynamic compressive stress–strain curves of bicrystals UC-B1 and CS-B1 are shown in Fig. 6(a). The flow stress of the specimens without pre-cyclic straining is pretty lower than the cycled one. There are 4 and 3 stress plateaus for specimens without pre-cyclic straining and after pre-cyclic straining, respectively. This is quite similar to the dynamic compressive stress–strain curves of single crystals, in which 3 stress plateaus can be observed for both with and without pre-cyclic strained specimens [26,39]. However, it is distinct from those for the annealed OFHC copper polycrystal tested at the same strain rate on the same SHPB apparatus (Fig. 6(c)), which has no plateaus that is also consistent with previous findings [40]. It is also different from the quasi-static compressive stress–strain curves for as grown single crystals and bicrystals in which no plateaus can be observed (Fig. 6(b)).

A possible explanation may be that in the dynamic compression tests of copper single crystals and bicrystals, with the increase of stress level, great number of slip planes, for exam-

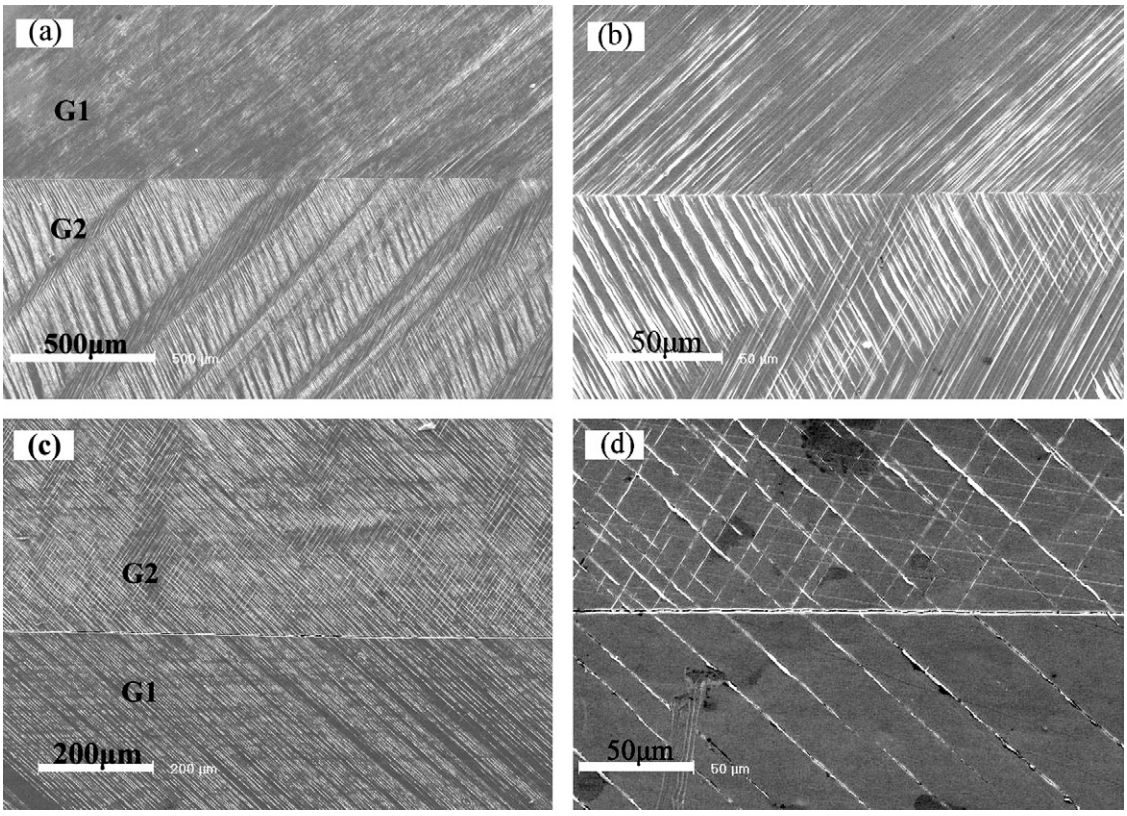

Fig. 4. Surface slip morphology after fatigue of (a) bicrystal B1, ε_{pl} 0.15%, 10^4 cycles, (b) bicrystal B1 with a higher magnification, (c) bicrystal B3, ε_{pl} 0.15%, 10^4 cycles, (d) bicrystal B3 with a high magnification. For all three bicrystals secondary slip is only observed in one side of the GB.

ple, the primary slip planes, can be activated simultaneously with an identical shear stress. Materials then turn into a flow state during which the stress maintains constant as the strain increases, until the planes are not geometrically favorable. After a while, the great number of secondary slip planes can also be activated simultaneously, and then the second plateau occurs. However, in the dynamic compression testing of polycrystals, the simultaneous activation of great number of slip planes with an identical critical shear stress will be impossible, because there are numerous grains with different orientations. Therefore, no stress plateaus can be observed for polycrystals (Fig. 6(c) and Ref. [40]). On the other hand, in the quasi-static compression testing of copper single crystals and bicrystals, the primary slip planes operate accumulatively and hence results in a hardening behavior and no plateau can be observed as shown in Fig. 6(b).

In the dynamic stress–strain curves of as grown copper single crystals, Li et al. [39] found that the ratio of the flow stresses of second plateau divided by that of first plateau is about 1.2. This is almost equal to the ratio of the Schmid factor Ω_{pri} for primary slip system divided by the second largest Schmid factor Ω_{sec} for secondary slip system. Therefore, the first plateau corresponds to the primary slip start-up and the second to the operation of secondary slip. A ratio parameter, R_Ω, can be proposed as following:

$$R_\Omega = \frac{\sigma_{Sec}/\sigma_{Fir}}{\Omega_{Pri}/\Omega_{Sec}} \quad (4)$$

Here, σ_{Fir} and σ_{Sec} represent the first and second plateau stresses, respectively. For as grown copper single crystals, R_Ω almost equals to 1. To confirm this phenomenon, we tested another as grown copper single crystal, whose dynamic compressive stress–strain curve is shown in Fig. 6(c), in which the R_Ω is 1.03. At the same strain rate of 4000 s^{-1} for fatigued copper single crystals, however, R_Ω differs from 1.11 to 1.22 [26], which is greater than that with as grown one. It is rational that in the fatigued crystals the secondary slip may be blocked to a certain extent by the existed primary dislocations or PSBs. So the formation of second stress plateau was suspended until an elevated stress level was gained.

In copper bicrystals with two component grains combined in parallel, situation becomes rather complex due to the orientation and GB effects. As first approximation, Eq. (1) can be used to estimate the average Schmid factors for the primary slip and secondary slip systems in bicrystals.

The average Schmid factor for primary slip systems in two component grains of the bicrystal, Ω_B, can be written as $\Omega_B = (V_{G1}/\Omega_{G1} + V_{G2}/\Omega_{G2})^{-1}$, in which $V_{G1} = V_{G2} = 0.5$, Ω_{G1} and Ω_{G1} are Schmid factors of primary slip systems in grain 1 and grain 2, respectively (Table 1). Similarly as above, the average Schmid factor of secondary slip systems, Ω'_B, can also be calculated as shown in Table 1. For bicrystals Eq. (4) then can be transformed as follows,

$$R^B_\Omega = \frac{\sigma_{Sec}/\sigma_{Fir}}{\Omega_B/\Omega'_B} \quad (5)$$

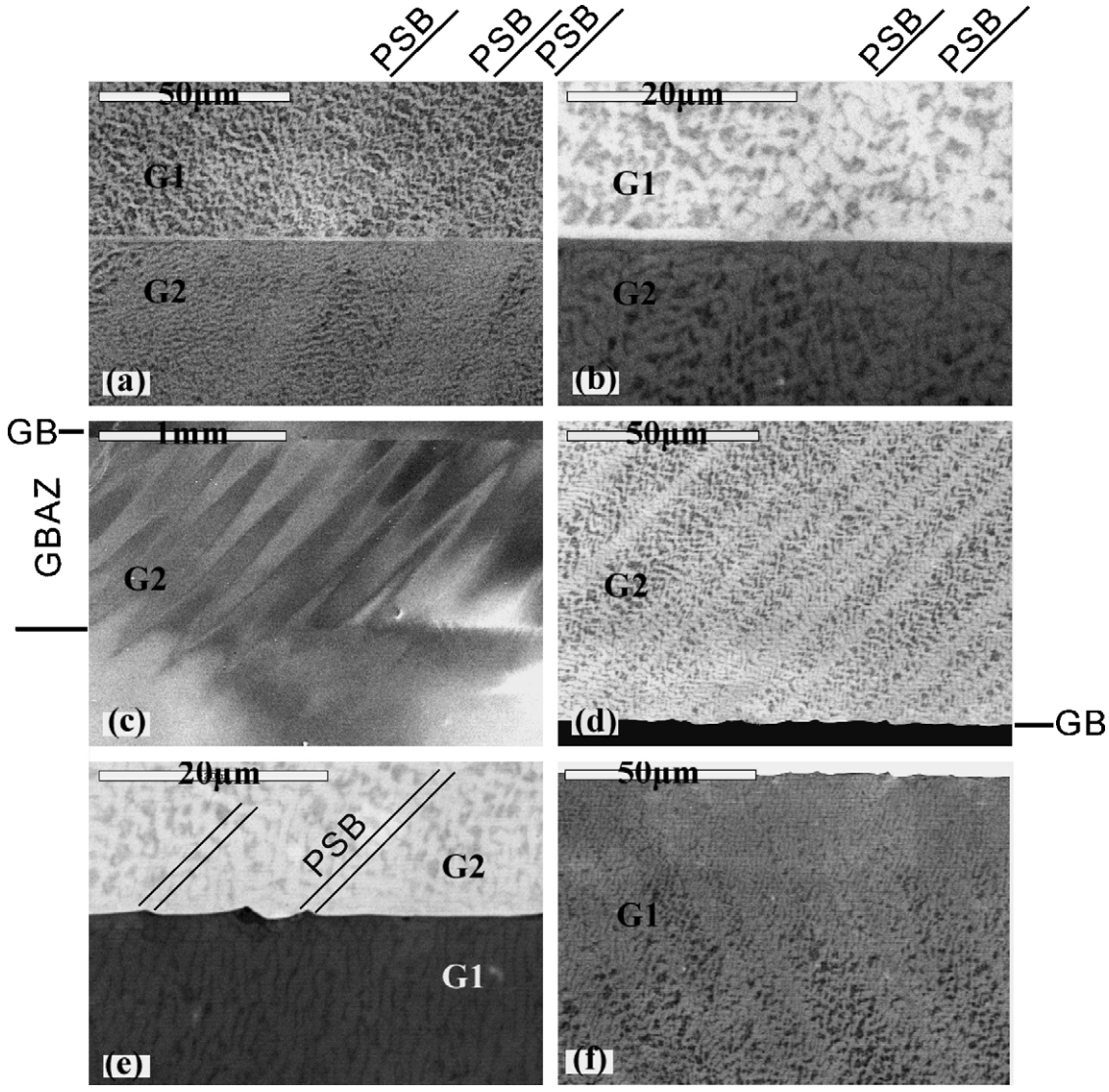

Fig. 5. Dislocation patterns near the grain boundary in bicrystals after fatigue and before dynamic tests. (a) Lower magnification of B1, (b) higher magnification of B1. (c) B1's GBAZ near the grain boundary. (d) Lower magnification of B2, in grain G2, the regular PSBs embedded in matrix veins. (e) Higher magnification of B2. (f) In the lower part of bicrystal B2, the irregular PSB structure appeared near the GB, and gradually turned into regular PSB structure away from GB.

At present, R_{Ω}^{B} of bicrystal UC-B1 is about 1.1. Similar to those in the copper single crystals, the first and second plateaus here also correspond to the operation of primary and secondary slip systems, respectively. The third and fourth plateaus may be due to the formation of GBAZ or ASBs.

For bicrystals with pre-cyclic straining, the first and second plateaus in dynamic stress–strain curves should also correspond to the operation of primary and secondary slip systems respectively. However, the values of R_{Ω}^{B} for CS-B1, CS-B2 and CS-B3 are 1.59, 1.34 and 1.52, respectively (Fig. 6(d)) that are much higher than those of single crystals and as grown bicrystals. It is conceivable that in the fatigued bicrystals, the activation of secondary slip systems needs much higher stress for the presence of GBAZ and abundant primary dislocations formed in the pre-cyclic straining. For comparison, the characteristics of compressive stress–strain curves of copper crystals are summarized as in Table 2.

Finally, the third plateau indicates the ASB formation and it will be discussed in the next section.

3.5. Formation of ASB and GB serrations after dynamic compression

3.5.1. Formation of ASBs

After dynamic tests, the specimens were examined with SEM-ECC technique. As shown in Figs. 7 and 8, ASBs were clearly observed to form in the pre-cyclic strained bicrystals. However, the ASB appearance in as grown bicrystals is not as clear as that in the pre-cyclic strained ones. Before impact, the 'CS' specimens contain PSBs and veins two-phase structures that are inhomogeneous and 'UC' specimens can be treated as a homogeneous structure. The results confirm that ASBs can be easily formed in the inhomogeneous materials, which is consistent with previous reports [20,41] and our recent results [26]. The

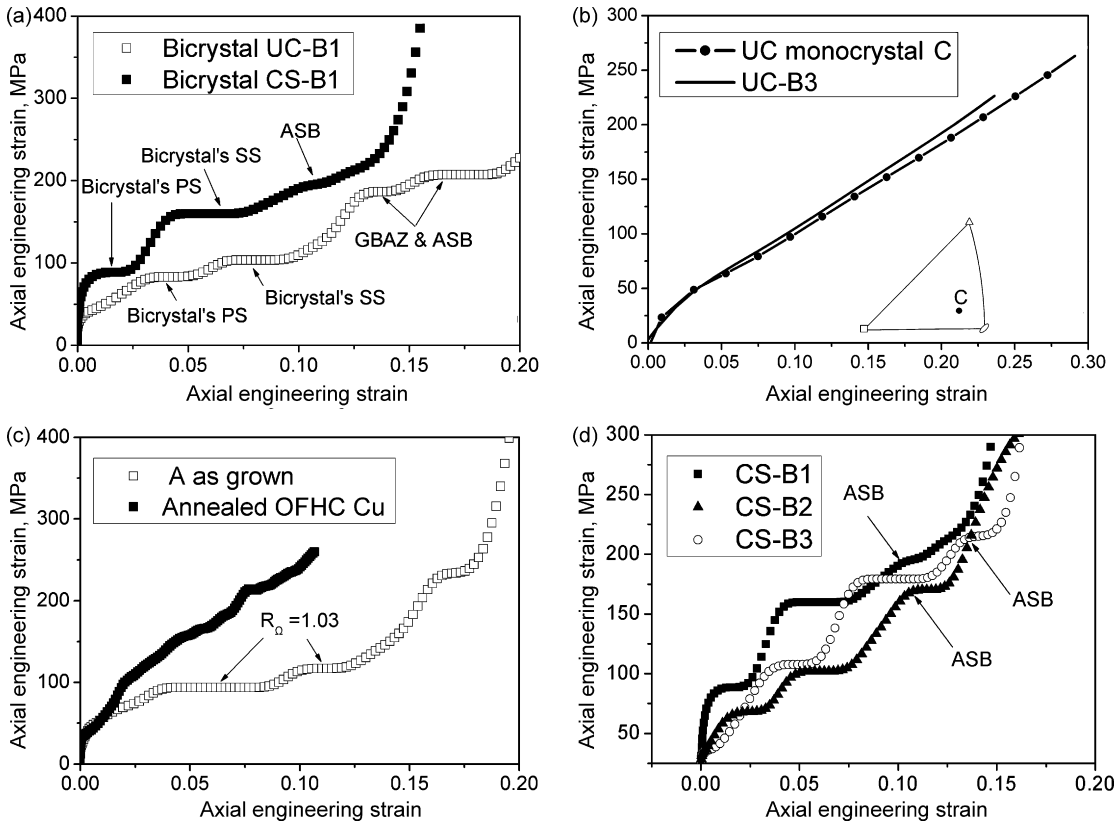

Fig. 6. (a) Dynamic stress–strain curves of bicrystal UC-B1 and CS-B1. (b) Quasi-static compressive stress–strain curve of as grown bicrystal B3 and single crystal C. (c) Dynamic stress–strain curves of annealed OFHC copper polycrystals and as grown single crystal A whose orientation $[\bar{1}\,2\,4]$ is identical with fatigued A of previous work [26]. (d) Dynamic stress–strain curves of the three bicrystals with pre-cyclic straining.

orientation of ASB plane in grain 1 of CS-B1 was determined to be parallel to $(\bar{7}\,4\,6)$ by analyzing the shearing traces on top and lateral surfaces. It should be noted that the ASB plane is not a habit plane, since various orientations of ASBs can be formed for different single crystals [26]. In addition, the ASB plane is not strictly a crystallographic plane due to the complexity of the ASB formation. Here, we use a crystallographic plane index to denote it for convenience. Fig. 9(a) illustrates the geometric relationships between ASB plane and primary slip plane (same as PSB plane) of sample CS-B1.

In previous study, the critical strain of ASB formation for fatigued single crystals with different orientations can be well determined by the start of the third plateau and it has been verified by post-deformation observation [26]. Here, the critical strains of ASB formation for pre-cyclic strained bicrystals can also be determined by this method. Taking the starting strain of the third plateau as the critical strain of ASB formation, they are 0.10, 0.11 and 0.14 for bicrystals B1, B2 and B3 respectively. A comparison between the critical strains for fatigued copper bicrystals and single crystals [26] is presented as follows.

Table 2
Characteristics of compressive stress–strain curves of copper crystals

No.	Materials	Loading rate (s^{-1})	Stress plateau	$\sigma_{Sec}/\sigma_{Fir}$	$\Omega_{Pri}/\Omega_{Sec}$ or Ω_B/Ω'_B	R_Ω or R^B_Ω	Ref.
1	As grown single crystal C	Quasi-static	No	–	–	–	Fig. 6(b)
2	As grown bicrystal B3	Quasi-static	No	–	–	–	
3	Annealed polycrystal	4×10^3	No	–	–	–	Fig. 6(c) and Ref. [40]
4	As grown single crystal	4×10^3	3	1.2 1.25	1.2 1.2	1 1.04	[39] Fig. 6(c)
5	Single crystal with pre-cyclic straining	4×10^3	3	1.33 1.58 1.25	1.2 1.29 1.08	1.11 1.22 1.16	Fig. 10 (a–c) in Ref. [26]
6	As grown bicrystal B1	4×10^3	4	1.25	1.13	1.1	Fig. 6(a)
7	Bicrystal with pre-cyclic straining	4×10^3	3	1.8 1.5 1.67	1.13 1.12 1.10	1.59 1.34 1.52	Fig. 6(d)

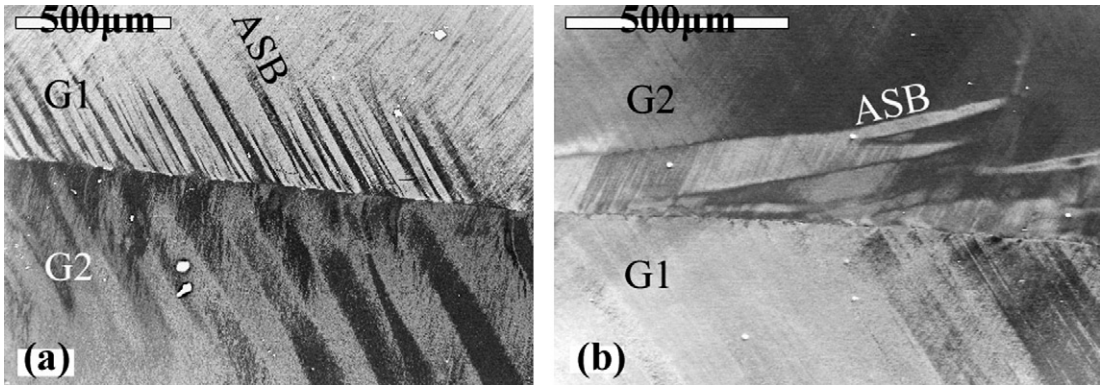

Fig. 7. ASBs are formed near the GB of pre-cyclic strained bicrystal (a) B1, (b) B3.

It is well known that during compression the loading axis will rotate towards [0 0 1]–[0 1 1] side in the stereographic triangle [42]. The rotation direction is determined by the great circle passing though the loading axis and [1 1 1] axis. The initial orientation of component G1 in bicrystal B1 is 12.3° away from [0 0 1]–[0 1 1] line. In Fig. 9(b), the horizontal axis represents this angle deviation and the vertical axis represents the critical strains in bicrystals and single crystals [26]. The figure shows that crystals with the same angle deviation have the same tendency for ASB formation no matter whether they are single crystals or bicrystal's component grains. However, the critical strains for ASB formation in the bicrystals are much smaller than

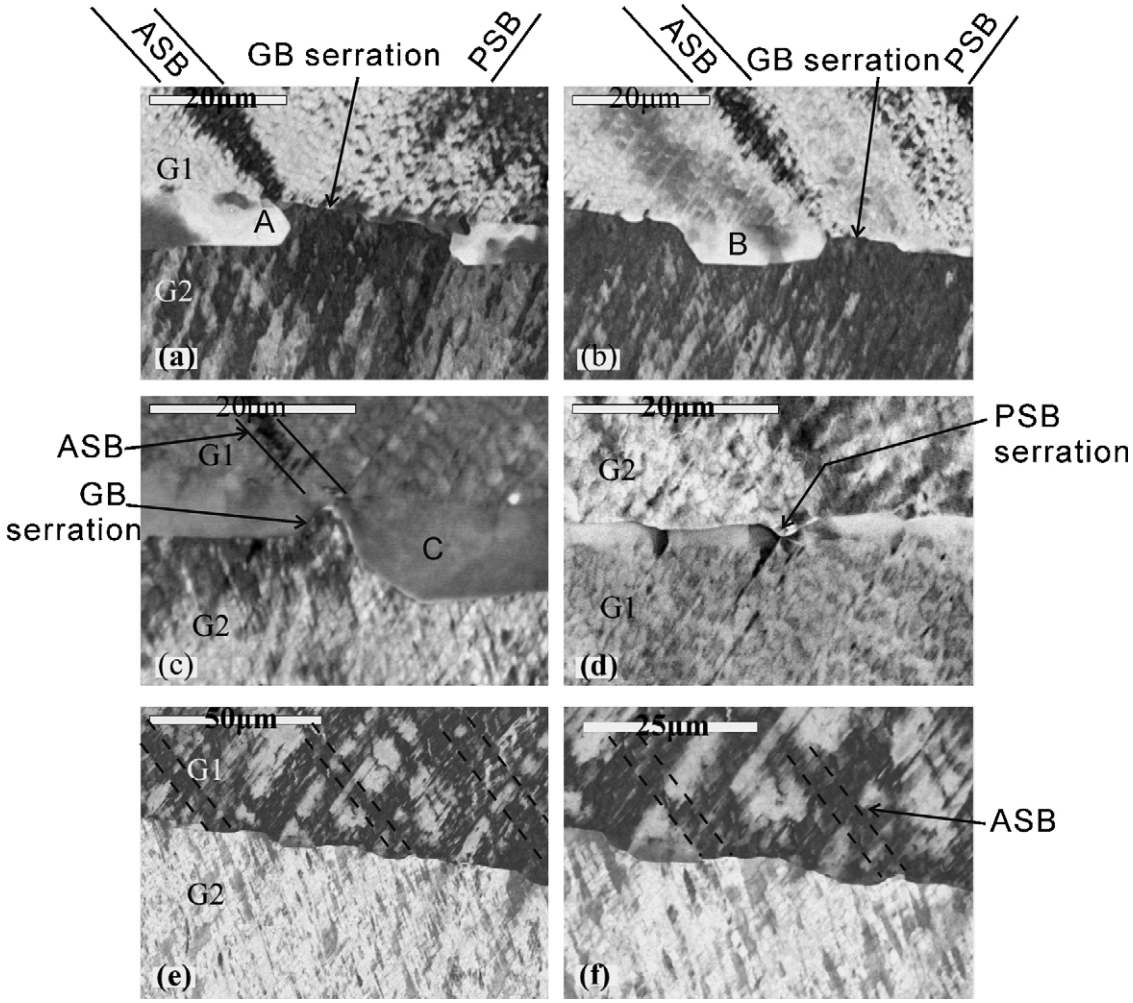

Fig. 8. The GB serrations and dislocation-free zones in: (a) specimen CS-B1-2 with impact strain $\varepsilon = -0.18$, (b and c) are the different regions of CS-B1-2, (d) PSB serrations in CS-B2-2 with impact strain $\varepsilon = -0.11$, (e) the GB morphology in UC-B1-2 sample with impact strain $\varepsilon = -0.20$, (f) the higher magnification of UC-B1-2.

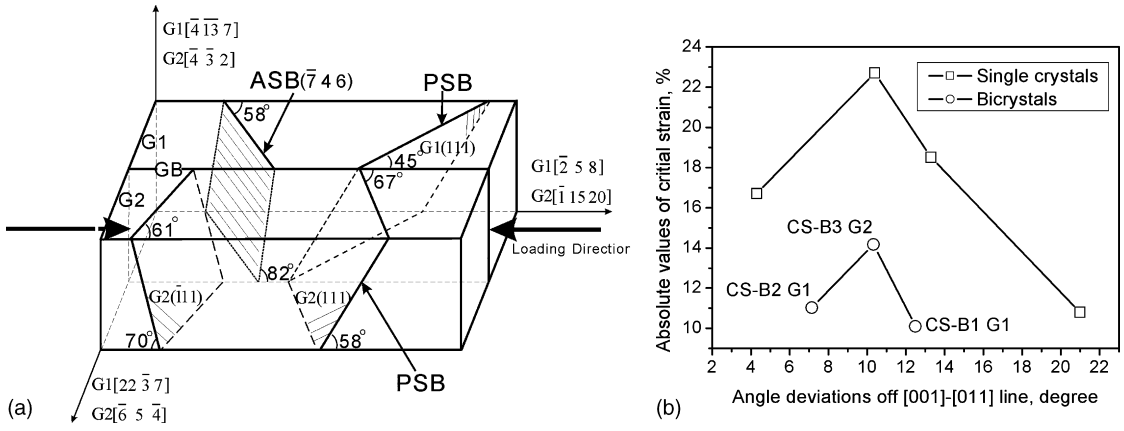

Fig. 9. (a) Schematic illustration of geometric relationships between ASB plane and primary slip plane (same as PSB plane) of CS-B1. (b) Comparisons of critical strains for ASB formation in fatigued bicrystals with those in single crystals [26].

those in single crystals. The reason probably rests on the stress concentration generated by the strain incompatibility near the GB. This stress concentration can effectively promote the ASB formation. Besides, in the present circumstance, ASBs were observed to extend only 1mm away from GB, see Fig. 7(a). A possible micro-mechanism for ASBs formation in monocrystal was proposed in our recent paper [26].

As mentioned above the third plateau of the bicrystals' dynamic stress–strain curves represents the ASBs' initiation and propagation. During this stage, ASB carries most of the strain; an equation then may be deduced:

$$\gamma_{\mathrm{pl}} = \gamma_{\mathrm{ASB}} f_{\mathrm{ASB}} \tag{6}$$

Here, γ_{pl} represents the total imposed shear strain. Since the axial strain range of the third plateau was about 0.02 for three bicrystals (see Fig. 6(d)), shear strain γ_{pl} then can be estimated to be 0.04. f_{ASB} is the volume fraction of ASBs and was measured to be about 0.17. So the shear strain of ASB (γ_{ASB}) in the present circumstance can be calculated to be 0.23. Based on the definition of simple shear, the angle deviation across an ASB with this degree of shear strain will be about 13° (arctan 0.23 = 13°).

OIM provides many details on the variation of the orientations of post-deformation microstructure, as shown in Fig. 10(a). In the center of an ASB the Schmid factor Ω is almost 0.5, which means the ASB is 'softer' to the present loading direction than the matrix. Similar to the soft phase of PSBs formed in cyclic straining. ASBs may carry most of the imposed strain at this stage. Besides, the misorientation from the edge to the center of an ASB was observed to be as large as 11°. This large lattice rotation also indicates the large shear strain carried by ASBs. In addition, the 11° large misorientation measured in OIM also agrees well with 13° shear angle calculated above.

3.5.2. GB serrations

After dynamic tests, GB serrations were clearly observed in 'CS' specimens. They correspond to the ASBs one by one and the average height is about 7 μm (Fig. 8(a–c)). However, in 'UC' specimens the ASBs are faint but still can be roughly

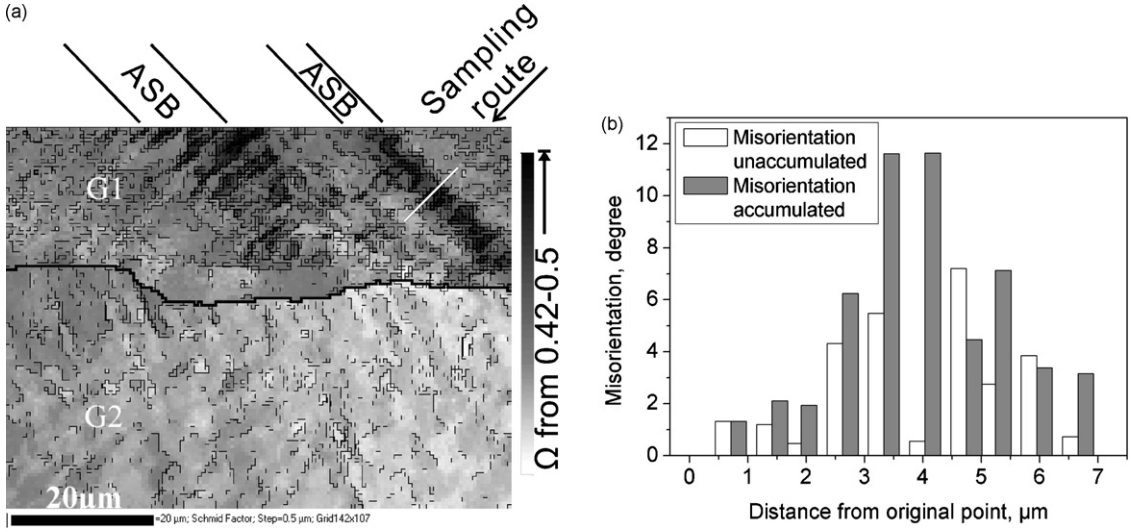

Fig. 10. (a) OIM near the GB of sample CS-B1-2 with step 0.5 μm, (b) the misorientation across an ASB. The misorientations accumulated are the orientation changes relative to the first point. The unaccumulated ones are those relative to the previous point.

distinguished. Correspondingly, the GB serrations can be observed and the average height is about 2–3 μm.

Before all the tests, the as grown GB is straight. After pre-cyclic straining, extrusions due to the shearing of PSBs can be measured to be about 1 μm (Fig. 5(e)). To estimate PSB extrusion in cyclic straining a model was established by Essmann et al. [43]. Under the assumption that all the interface dislocations arriving at the surface, the PSB lamella elongation e (the PSB extrusion) in the direction of the active slip vector can be calculated by,

$$e = \frac{C_V^{sat} d}{\cos(\beta)} \tag{7}$$

Here, d denotes the sample diameter, β the angle between loading axis and the normal to the active slip plane and C_V^{sat} is the saturation concentration of vacancies in the fatigued copper crystals. The interface dislocations refer to the edge dislocations which have been deposited at the interface between matrix and PSBs. In case of copper after cyclic saturation, $C_V^{sat} = 2.7 \times 10^{-4}$ [43] and at present $d = 2.5$ mm, $\cos\beta = 0.66$. Substituting these values into Eq. (7), $e = 1.02$ μm can be obtained. This result agrees well with the height of PSB-GB extrusions shown in Fig. 5(e).

During the dynamic tests, the deformation process may be that: at the early stage, the existed and newly formed interface dislocations (deposited at the interface between matrix and PSBs) of the primary slip system activated simultaneously, forming PSB-GB serrations (Fig. 8(d)). Then secondary slip started. Once ASB had initialed at the third stage, large-scale GB serrations started to form and the shape of serrations became multi-sided. Two shearing directions that are along PSBs and ASBs can be clearly distinguished, see Fig. 8(a and c). In addition, the height of serrations was enlarged due to the intense shear localization of ASBs.

In OIM, no clear evidence of recrystallization was observed along the GB or in the ASBs. The regions adjacent to GB serration, for example, regions A–C in Fig. 8(a–c), respectively, are similar to the recrystallization grains in appearance. However, OIM indicates that it is not the case because the misorientation across the upper boundary of these regions is less than 2°. On the other hand, it is similar to the dislocation-free zones formed in cyclic straining [44–45]. The process may be that in the dynamic tests the dislocations in the region adjacent to a GB serration were swept into the GB leaving this dislocation-free zone behind.

4. Conclusions

In the present paper, the saturation stress acting at GBAZ during cyclic straining was calculated to be higher than that in the grain interior. In addition, the initial hardening rates of bicrystals are also higher than the mean value of those of each component grains.

There are three plateaus in the dynamic compressive stress–strain curves in copper bicrystals with pre-cyclic straining. The first and second plateaus correspond to the simultaneous operation of the primary and secondary slips, respectively, and the third to the ASB formation. Experimental results indicate that the critical strains of ASB formation in the bicrystals are much smaller than those in single crystals. However, the crystals with the same orientation have the same tendency for ASB formation no matter whether they are single crystals or bicrystal's component grains. Large lattice rotations occurred across the ASBs and large-scale GB serrations were also observed. They are all due to the intense shear localization of ASBs.

Acknowledgements

The authors would like to thank Prof. Shen L.T. and Chen S.X., Institute of Mechanics, CAS, Beijing, for their help in dynamic testing. Professor Su H.H. and Gao W. kindly assisted us in ECC and OIM observations. The work was financially supported by NSFC under Grant No. 50471082.

References

[1] J.D. Livingston, B. Chalmers, Acta Metall. 5 (1957) 322.
[2] C. Elbaum, Trans. TMS-AIME 218 (1960) 444.
[3] J.J. Hauser, B. Chalmers, Acta Metall. 9 (1961) 802.
[4] R.E. Hook, J.P. Hirth, Acta Metall. 15 (1967) 535.
[5] J.P. Hirth, Met. Trans. 3 (1972) 3047.
[6] S. Miura, K. Hamashima, K.T. Aust, Acta Metall. 28 (1980) 1591.
[7] E.V. Esquivel, L.E. Murr, Mater. Sci. Eng. A409 (2005) 13.
[8] C. Rey, A. Zaoui, Acta Metall. 30 (1982) 523.
[9] S.X. Li, R.Q. Chu, J.Y. Hou, Z.G. Wang, Philos. Mag. A77 (1998) 1081.
[10] V. Paidar, P.P. Pal-val, S. Kadeckova, Acta Metall. 34 (1986) 2277.
[11] V. Paidar, J. Gemperlova, P.P. Pal-val, Mater. Sci. Eng. A137 (1991) 69.
[12] Y.M. Hu, Z.G. Wang, G.Y. Li, Scripta Mater. 34 (1996) 331.
[13] Z.F. Zhang, Z.G. Wang, Acta Mater. 46 (1998) 5063.
[14] Z.F. Zhang, Z.G. Wang, Y.M. Hu, Mater. Sci. Eng. A272 (1999) 410.
[15] Z.F. Zhang, Z.G. Wang, Acta Mater. 51 (2003) 347.
[16] C.L. Wittman, M.A. Meyers, H.R. Pak, Metall. Trans. A21 (1990) 707.
[17] M.A. Meyers, C.L. Wittman, Metall. Trans. A21 (1990) 3153.
[18] A.K. Zurek, Metall. Mater. Trans. 25 (1994) 2483.
[19] D.S. Kim, S. Nemat-Nasser, J.B. Isaacs, D. Lischer, Mech. Mater. 28 (1998) 227.
[20] H. Feng, M.N. Bassim, Mater. Sci. Eng. A266 (1999) 255.
[21] C.G. Lee, W.J. Park, S. Lee, K.S. Shin, Metall. Mater. Trans. A29 (1998) 477.
[22] M.A. Meyers, V.F. Nesterenko, J.C. LaSalvia, Q. Xue, Mater. Sci. Eng. A317 (2001) 204.
[23] Z.Q. Duan, S.X. Li, D.W. Huang, Fatigue Fract. Eng. Mater. Struct. 26 (2003) 1119.
[24] G.Q. Cheng, S.X. Li, Mater. Sci. Technol. 21 (2005) 813.
[25] H. Miura, M. Ozama, R. Mogawa, T. Sakai, Scripta Mater. 48 (2003) 1501.
[26] S.X. Li, R.Q. Yang, J.W. Li, Z.F. Zhang, Philos. Mag. 86 (2006) 5769.
[27] H. Mughrabi, Mater. Sci. Eng. 33 (1978) 207.
[28] A.S. Cheng, C. Laird, Mater. Sci. Eng. 51 (1981) 111.
[29] Z.S. Basinski, S.J. Basinski, Prog. Mater. Sci. 36 (1992) 89.
[30] P. Lukas, L. Kunz, Mater. Sci. Eng. 47 (1985) L1.
[31] B. Gong, Z.G. Wang, Y.W. Zhang, Mater. Sci. Eng. A194 (1995) 171.
[32] Y.M. Hu, Z.G. Wang, G.Y. Li, Mater. Sci. Eng. A208 (1996) 260.
[33] B. Gong, Z.R. Wang, Z.G. Wang, Acta Mater. 45 (1997) 1365.
[34] X.W. Li, Z.G. Wang, S.X. Li, Mater. Sci. Eng. A265 (1999) 18.
[35] X.W. Li, Z.G. Wang, S.X. Li, Mater. Sci. Eng. A269 (1999) 166.
[36] D. Kuhlmann-Wilsdorf, C. Laird, Mater. Sci. Eng. 27 (1977) 137.
[37] A.T. Winter, Philos. Mag. A37 (1978) 457.

[38] B. Gong, Z.R. Wang, Z.G. Wang, Y.W. Zhang, Mater. Sci. Eng. A210 (1996) 94.
[39] J.W. Li, Master Degree Thesis, Institute of Metal Research CAS, 2004 (in Chinese).
[40] S. Nemat-Nasser, Y.L. Li, Acta Mater. 46 (1998) 565.
[41] M.M. Rashid, G.T. Gray, S. Nemat-Nasser, Philos. Mag. A65 (1992) 707.
[42] C.N. Reid, Deformation Geometry for Materials Scientists, Pergamon Press, 1973.
[43] U. Essmann, U. Gosele, H. Mughrabi, Philos. Mag. A44 (1981) 405.
[44] A.T. Winter, O.B. Pederson, K.V. Rasmussen, Acta Metall. 29 (1981) 735.
[45] J.I. Dickson, S. Turenne, H. Bande, G. L'esperance, Mater. Sci. Eng. 89 (1987) L31.